ADVANCED QUANTUM TECHNOLOGIES
www.advquantumtech.com

Nano-Cavity QED with Tunable Nano-Tip Interaction

Molly A. May, David Fialkow, Tong Wu, Kyoung-Duck Park, Haixu Leng, Jaron A. Kropp, Theodosia Gougousi, Philippe Lalanne, Matthew Pelton, and Markus B. Raschke**

Quantum state control of two-level emitters is fundamental for many information processing, metrology, and sensing applications. However, quantum-coherent photonic control of solid-state emitters has traditionally been limited to cryogenic environments, which are not compatible with implementation in scalable, broadly distributed technologies. In contrast, plasmonic nano-cavities with deep sub-wavelength mode volumes have recently emerged as a path toward room temperature quantum control. However, optimization, control, and modeling of the cavity mode volume are still in their infancy. Here recent demonstrations of plasmonic tip-enhanced strong coupling (TESC) with a configurable nano-tip cavity are extended to perform a systematic experimental investigation of the cavity-emitter interaction strength and its dependence on tip position, augmented by modeling based on both classical electrodynamics and a quasinormal mode framework. Based on this work, a perspective for nano-cavity optics is provided as a promising tool for room temperature control of quantum coherent interactions that could spark new innovations in fields from quantum information and quantum sensing to quantum chemistry and molecular opto-mechanics.

1. Introduction

Optical cavities are important tools to enhance and control light–matter interactions for applications from quantum information, metrology, and sensing to quantum photochemistry.[1–5] Traditionally, the cavity–emitter interaction strength has been limited by relatively large, diffraction-limited cavity mode volumes. In these systems, low temperature operation is generally required to sufficiently decouple emitters from their environment and reduce their dephasing rate below that of the cavity–emitter coupling strength. However, a new regime of strong cavity–emitter interaction has recently been established using plasmonic nano-cavities with deep sub-diffraction-limited mode volumes.[6–10] While plasmonic nanocavities extend quantum state control even to room temperature, this approach has relied largely on nano-fabrication techniques to generate static plasmonic cavities, which limit the ability to tune, control, and image emitters in the strong coupling regime. Due to these constraints, a systematic understanding of the interrelation between coupling strength, cavity mode volume, and relative cavity–emitter position on the spatio-spectral properties of the nano-cavity emitter coupled system is lacking, and this has limited the systematic development of a broader application space. Furthermore, established theories for the determination of cavity mode volume do not always predict the behavior of non-Hermitian, or lossy, plasmonic cavities.[11,12] While theories for modeling plasmonic cavity mode volumes have been proposed,[11–14] questions remain[11,15] calling for more precise measurements to inform further theoretical developments.

In order to overcome this bottleneck of static plasmonic nanocavities, we recently developed a new approach to configurable plasmonic nano-cavity quantum electrodynamics (cQED). Using the optical antenna properties of a plasmonic nano-tip in a scanning near-field optical microscope, we demonstrated strong coupling to a single quantum dot (QD) at room temperature with photoluminescence (PL) state read-out.[9]

Here, following a review of cQED in its extension to the nanoscale, we describe new experiments in which we apply tip-enhanced strong coupling (TESC) to optimize the coupling strength between a plasmonic cavity and a single quantum emitter. We probe the mode dispersion of the hybrid cavity–emitter state over a 3D parameter space. We then image the spatial

Dr. M. A. May, Prof. K.-D. Park, Prof. M. B. Raschke
Department of Physics
Department of Chemistry, and JILA
University of Colorado
2000 Colorado Ave., Boulder, CO 80309, USA
E-mail: markus.raschke@colorado.edu

D. Fialkow, Dr. H. Leng, J. A. Kropp, Prof. T. Gougousi, Prof. M. Pelton
Department of Physics
UMBC (University of Maryland, Baltimore County)
Baltimore, MD 21250, USA
E-mail: mpelton@umbc.edu

Dr. T. Wu, Prof. P. Lalanne
Numérique et Nanosciences (LP2N)
Laboratoire Photonique
IOGS, CNRS, Univ. Bordeaux
33400 Talence, France
E-mail: tong.wu@institutoptique.fr

Prof. K.-D. Park
Department of Physics
School of Natural Sciences
Ulsan National Institute of Science and Technology
50 UNIST-gil, Eonyang-eup, Ulju-gun, Ulsan, South Korea

The ORCID identification number(s) for the author(s) of this article can be found under https://doi.org/10.1002/qute.201900087

DOI: 10.1002/qute.201900087

dependence of the coupling strength due to changes in the cavity geometry as the tip is scanned in relation to a single QD along both the lateral and vertical directions. Furthermore, for a deeper understanding of our previous results, we compare these results to theoretical predictions based on both a classical Maxwell's equation solver and recently established techniques for the normalization of leaky resonator modes in a quasinormal-mode formalism for a rigorous definition of the plasmonic cavity mode volume and its spatial dependence.[11]

2. Background

When spontaneous emission of a two level system was established by Einstein as a necessary mechanism for maintaining thermal equilibrium, it was initially believed to be an irreversible process in which the excited state energy is permanently lost to the infinite bath of available vacuum states.[16,17] However, the subsequent development of cQED showed that spontaneous emission can be enhanced, suppressed, and even reversibly exchanged with a photonic cavity.

To understand these developments, we begin with the vacuum interaction of light with a two level system which undergoes spontaneous emission from excited state $|e\rangle$ to its ground state $|g\rangle$, accompanied by the emission of a photon with energy $E_e - E_g = \hbar\omega$. Spontaneous emission is mediated by interactions with vacuum electromagnetic field modes that have zero-point energy $\hbar\omega/2$ and root mean square electric field $E_{\text{vac}} = \sqrt{\frac{\hbar\omega}{2\epsilon_0 V}}$ for a mode with frequency ω, quantized over an arbitrary volume V and permittivity of free space ϵ_0. The rate of energy exchange between an individual vacuum mode and a two level system is given by the vacuum Rabi frequency $\Omega = \vec{\mu}_{\text{eg}} \cdot \vec{E}_{\text{vac}}/\hbar$ for the electric dipole matrix element $\vec{\mu}_{\text{eg}} = \langle g|H'|e\rangle$ between the ground $\langle g|$ and excited state $|e\rangle$. By integrating over a continuum of unoccupied vacuum modes, the spontaneous emission rate $\Gamma_{\text{e}\to\text{g}}$ of the emitter into a vacuum mode can be described by Fermi's golden rule

$$\Gamma_{\text{e}\to\text{g}} = 2\pi\Omega_{\text{eg}}^2 \frac{\rho(E_g)}{3} \tag{1}$$

where $\rho(E_g)$ is the local density of states (LDOS) at the energy E_g of the final state, which for vacuum is given by $\rho_{\text{vac}} = \omega^2/\pi^2c^2$.[17]

Edward Purcell subsequently noted that an emitter's vacuum spontaneous emission rate can be modified by placing the emitter in an environment with a modified density of states ρ_{cav} compared to that of the vacuum ρ_0.[18,19] (This idea was originally presented in the context of nuclear magnetic resonance, but applies to any radiative transition.) This modified LDOS in a dielectric environment can be calculated using the Green's function for the electric field generated by a dipole at the position of the dipole itself. In other words, it arises from the electric field that an emitter generates at its own position in space, and this self-field can be modified by placing the emitter in an environment that modifies the electromagnetic density of states.[20] The modification of the spontaneous relaxation, or emission rate for a single resonant cavity mode due to the modified LDOS ρ_{cav} is quantified by the Purcell Factor

$$F_P = \frac{\rho_{\text{cav}}}{\rho_0} = \frac{\Gamma_{\text{cav}}}{\Gamma_0} \tag{2}$$

where Γ_{cav} and Γ_0 are the modified and vacuum emission rates, respectively. This effect was first demonstrated by Karl Drexhage at optical frequencies in his pioneering experiments on fluorescent molecules on dielectric films over a metallic surface, but the open geometry of his experiment only allowed for moderate modification of the spontaneous emission rate.[21]

As fabrication techniques and methods for isolating and measuring the state of emitters improved, high Q cavities were developed that could achieve both enhancement and suppression of spontaneous emission rates by factors of up to 500.[22–26] The Purcell factor can be re-derived in this regime in terms of the relevant parameters for a resonant cavity mode:

$$F_P = \frac{3Q}{4\pi^2}\left(\frac{\lambda_0}{n}\right)^3 \text{Re}\left(\frac{1}{\tilde{V}}\right) \tag{3}$$

where $\lambda_0 = 2\pi c/\omega_{\text{cav}}$ is the wavelength corresponding to the cavity resonance, n is the refractive index, $Q = \omega_{\text{cav}}/\Delta\omega_{\text{cav}}$ is the quality factor of the resonance mode with frequency $\omega_{\text{cav}}(1 - i/2Q)$, linewidth $\Delta\omega_{\text{cav}}$, and complex mode volume $\tilde{V} = V' + iV''$. In the limit of very high Q factors, the modal electric fields are real, which leads to real $\tilde{V}$ values, and Equation (3) can be reduced to the usual formula defined in common textbooks of Hermitian cavities.[11] Early cQED experiments employed a variety of cavity geometries to optimize F_P, ranging from parallel flat mirrors[24–26] to spherical mirrors in a Fabry–Perot geometry which reduced diffractive edge effects and significantly increased Q,[23,27] to more complex microwave cavity designs.[22] However, the behavior of a two-level system in a cavity is determined by the ratio of the Rabi frequency to the loss rate of the system Ω/κ, where κ includes radiative and nonradiative loss rates from both the cavity and the emitter ($\gamma_{\text{r}}^{\text{cav/EM}}$ and $\gamma_{\text{nr}}^{\text{cav/EM}}$), and these experiments were still operating in a regime where emitted photons were lost due to cavity absorption and leakage at a rate greater than 10 times the rate of absorption by the emitter.[23]

The achievement of coherent energy exchange between cavity and emitter at a rate larger than it is lost to the environment, called the strong coupling regime, was a landmark achievement of the late 1980s.[28–32] This advance in cavity optics enabled investigation of the light confined in a cavity and its interaction with atoms or other particles in a regime where the quantum nature of light is significant. This phenomenon is characterized by the Rabi oscillation of the excited state population where the emitter re-absorbs its own emitted photon in an energy conserving exchange with the cavity.

This single emitter (EM), single photon field (F) interaction in the rotating wave approximation, ignoring the vacuum field energy and dissipation processes like nonradiative decay of the emitter and cavity leakage is described by the Jaynes–Cummings Hamiltonian,

$$\begin{aligned} H &= H_{\text{EM}} + H_{\text{F}} + H_{\text{EM/F}} \\ &= \hbar\omega_{\text{EM}}\sigma^\dagger\sigma + \hbar\omega_{\text{cav}}a^\dagger a + \hbar g(\sigma a^\dagger + \sigma^\dagger a). \end{aligned} \tag{4}$$

Here, $\hbar\omega_{\text{EM}}\sigma^\dagger\sigma$ is the energy corresponding to the emitter excitation for emitter transition frequency ω_{EM}, emitter excitation raising operator $\sigma^\dagger$, and emitter excitation lowering operator σ. The cavity field energy is described by $\hbar\omega_{\text{cav}}a^\dagger a$ for cavity photon

raising operator $a^\dagger$ and lowering operator a and the interaction energy is given by $H_{\mathrm{EM/F}} = \hbar g(\sigma a^\dagger + \sigma^\dagger a)$ where g is the atom-field coupling energy in the single photon limit, which is often called the cavity QED coupling constant. This coupling energy is defined as

$$\hbar g(r) := -\sqrt{\frac{\hbar\omega_{\mathrm{cav}}}{2\epsilon_0}}\vec{\mu}_{\mathrm{eg}} \cdot \mathbf{f}(\mathbf{r}) \tag{5}$$

for permittivity of the cavity volume ϵ_0, where $\mathbf{f}(\mathbf{r})$ is the normalized spatial mode profile of the single photon electric field

$$\mathbf{E}(\mathbf{r}) = -\sqrt{\frac{\hbar\omega_{\mathrm{cav}}}{2\epsilon_0}}[\mathbf{f}(\mathbf{r})a + \mathbf{f}^*(\mathbf{r})a^\dagger]. \tag{6}$$

Then, applying field normalization

$$\int d^3r|\mathbf{f}(\mathbf{r})|^2 = 1, \tag{7}$$

this leads to an inverse square root relationship between g and the cavity volume V'

$$g = -\hat{\epsilon} \cdot \vec{\mu}_{\mathrm{eg}}\sqrt{\frac{\omega_{\mathrm{cav}}}{2\epsilon_0\hbar V'}} \tag{8}$$

where $\hat{\epsilon}$ is the polarization unit vector of the applied field. This indicates that for strong coupling, the emitter must have a large, cavity-aligned transition dipole moment and a small V', which is important for plasmonic cavities which rely on highly confined cavity volumes to achieve large coupling strengths.

The Jaynes–Cummings light–matter interaction Hamiltonian predicts quantum mode hybridization which leads to new eigen states that are given by

$$|\pm\rangle_n = \frac{1}{\sqrt{2}}(|g, n+1\rangle \pm |e, n\rangle) \tag{9}$$

with energies for resonant conditions, and ignoring the vacuum field energy

$$E_{\pm_n} = \hbar\omega_{\mathrm{cav}}\left(n \pm \frac{\hbar g}{2}\sqrt{n+1}\right) \tag{10}$$

where g and e are the ground and excited states of the emitter n is the number of excitations in the cavity, and the new states are split compared to the unhybridized modes by an energy $\hbar g\sqrt{n+1}$. These new eigenstates were referred to as upper ($|UP\rangle$) and lower ($|LP\rangle$) polariton branches in experiments that involved a continuum of cavity and emitter modes.[33–37]. This predicted energy splitting which scales with the square root of the cavity photon number n is often referred to as the Jaynes–Cummings ladder.

This energy splitting corresponds to dynamic oscillations in the emitter's intensity at the Rabi frequency

$$\Omega_R = \sqrt{4(n+1)g^2 + \Delta^2} \tag{11}$$

where $\Delta = \omega_{\mathrm{cav}} - \omega_{\mathrm{EM}}$ is the cavity detuning from the emitter resonance. For a resonant cavity and a single excitation, this reduces to $\Omega_{\mathrm{R}} = 2g$. Due to this relationship, g is referred to as the vacuum Rabi frequency (although note the difference in convention of a factor of 2).

While free space cavities were being optimized for interactions with atoms, a variety of other cavity–emitter systems were simultaneously being explored. For example, solid state cavities are formed using distributed Bragg reflectors to create high Q and low volume Fabry–Perot resonators[38–40] or by using whispering gallery modes in ring and disk geometries.[41,42] These designs are capable of achieving diffraction limited mode volumes, but cavities with diffraction-limited mode volumes are still limited to single photon coupling strengths of $g \lesssim 100\ \mu$eV for emitters with resonances in the visible spectrum and dipole moments characteristic of atomic and molecular emitters (≈ 1 Debye). Thus, to achieve the coupling-to-loss ratios required for the strong coupling regime in the single photon limit, that is, $g \propto \mu_{\mathrm{eg}}\sqrt{\frac{\omega_{\mathrm{cav}}}{\bar{V}}} > \kappa/4$, these cavities must have very low losses corresponding to $Q \geq 1{,}000$. Furthermore, sufficiently low emitter loss rates γ^{EM} are also required, corresponding to a narrow emitter linewidth $\Delta\omega_{\mathrm{EM}}$. This leads to a technical challenge for achieving spectral mode overlap, but more importantly, cryogenic temperatures are generally required to reduce dephasing and decrease $\Delta\omega_{\mathrm{EM}}$. The need for cryogenic conditions may limit broader applications and scalability of quantum technologies, making room temperature solutions desirable for broad use of chip-based quantum sensors and quantum logic devices.

The three orders of magnitude difference in length scale between visible light and single quantum emitters like atoms, molecules, semiconducting quantum dots, and atom-like defect centers,[43] leads to a fundamental limit of the light–matter interaction strength for weakly confined fields like those in diffraction-limited cavities.[44–46] To aid in the transduction of propagating electromagnetic radiation into localized forms of energy, optical antennas were developed in the form of metallic nanostructures that resemble models established for microwave and radio antennas.[46,47] However, few-fs Drude relaxation and radiative decay for metals at optical frequencies lead to significant ohmic loss corresponding to $Q \approx 5 - 50$. To compensate for their high loss rates, optical antennas take advantage of resonant electron charge density oscillations, called surface plasmon resonances or surface plasmon polaritons (SPPs), that are generated in metal nanostructures in the presence of oscillating electric fields. While these SPPs undergo fast decay, they also lead to a sharp increase in the LDOS that can be used to achieve optical field localization in the evanescent regime. The localization length l_{loc} primarily scales with the size and geometric parameters of the nanostructure, making optical antennas a powerful tool for imaging with resolution below the diffraction limit, especially at infrared wavelengths.[48–50]

In this framework, an optical antenna is treated as a passive element that enhances the transition rate of an emitter through an increase in the LDOS as described by Equation (2), but does not change its intrinsic properties. However, the optical field localization created by SPPs leads to nanoscopic mode volumes which can overcome the large ohmic loss rates of plasmonic cavities and mediate interactions analogous to those facilitated by optical cavities and for sufficient coupling to loss ratios, hybridization of the cavity and emitter wave functions can be achieved.

Recently, plasmonic nano-antenna cavities in the form of highly polarizable metallic nanostructures with dimensions down to just a few nanometers,[7,51] which allow for deep sub-diffraction limited mode volumes, have been broadly employed to generate hybrid quantum states of plasmons and emitters.[52] The increased interaction rate facilitated by these nanoscopic cavity mode volumes have enabled strong coupling to both ensembles and single emitters at room temperature.[7–10,51,53]

Plasmonic cavities take advantage of evanescent near-field radiation that is highly confined near metallic surfaces, which is in contrast to traditional cavities which confine far-field propagating photons between two mirrors or in dielectric materials. Nevertheless, while the function of these cavities are not strictly the same, they lead to the same light–matter interaction Hamiltonian and can be treated in the same formalism. It is worth noting, however, that while simulations based on Maxwell's equations confirm that the electric field in common plasmonic cavity designs is confined to a nanoscopic volume, calculation of a specific value of $\tilde{V}$ must be handled with care in these highly dissipative, non-Hermitian systems. In this regime, modes become complex fields and their frequencies also become complex, as described earlier, making $\tilde{V}$ a complex number containing information about the local phase shift of the mode compared to that of the cavity which is related to the loss rate κ.[11,12]

Working in this plasmonic near-field regime provides several advantages. For example, much of the loss from plasmonic cavities tends to be radiative, which facilitates high signal-to-noise optical detection. Furthermore, their broad linewidths can easily be overlapped with emitter modes, and they facilitate large coupling strengths that can overcome loss rates even for room temperature operation.

Many plasmonic cavity strong coupling studies have relied on multiple (n_{em}) emitters in the form of, for example, J-aggregates[54] to increase the coupling strength through a large collective effect ($\Omega_{\mathrm{R}} \propto \sqrt{n_{\mathrm{em}}/V'}$). However, experiments involving multiple emitters are impracticable for some applications in quantum gates[55] and entanglement[56] because they exhibit an equidistant energy spectrum that is identical to that of a classical system. By contrast, a single emitter strongly coupled to a cavity exhibits single photon nonlinearities such as the Jaynes Cummings ladder and photon blockade effects.[4,57]

The observation of strong couping of single emitters to plasmonic cavities at room temperature was first demonstrated through Rabi splitting in scattering spectra.[6] However, observation of multiple peaks in the scattering signal is not sufficient to ensure strong coupling, as other effects like Fano-like interference can lead to nearly identical spectral features.[54] Over the past two years, strongly coupled plexciton states were observed in the emission of single emitters coupled to plasmonic cavities in several experiments at room temperature. Most of these employed nanoparticle-on-a-mirror (NPoM) geometry in which an emitter is located between a metal nanoparticle and a planar metal substrate.[7–10] This is a significant landmark for the field, as this modality provides unambiguous evidence of strong coupling and paves the way for new applications in single emitter quantum information and photonic quantum devices.

However, while significant progress has been made in extending single emitter strong coupling to scalable, room temperature platforms based on plasmonic nano-cavities with deep sub-diffraction-limited mode volumes,[6–10] this approach has focused primarily on the fabrication and implementation of static plasmonic cavities, which do not allow for imaging, optimization, or control of the spatially dependent cavity–emitter interaction strength. Indeed, recent work on a quantum dot coupled to a scanning plasmonic slot structure suggests evidence for reaching the strong coupling regime in single emitter PL at room temperature,[8] yet is plagued by convoluted spectra with large background and competing artefacts due to charged exciton emission.

These limitations are addressed by TESC,[9] which employs a simplified approach based on the optical antenna properties of scanning plasmonic nano-tip structures.[58–62] Optical antennas in the form of AFM tips have previously been demonstrated as a powerful platform for controlling the optical properties of materials on the nanoscale from dark exciton emission to optical tuning via induced strain,[63,64] and their utility can be further improved by employing a tilted tip geometry, as shown in **Figure 1**a, which leads to plasmonic vector field control and enhancement of both in-plane and out-of-plane dipole moments and maximizes optical confinement.[65] With these innovations, and with the ability to configure the nano-tip cavity for maximum coupling strength, we achieve single-emitter coupling that is comparable to the strongest coupling seen in PL, even from large ensembles of emitters,[7,54,66] with the added ability to control the cavity coupling and mode volume through tip placement and to couple a series of different single quantum emitters to the same cavity.

3. Experimental Section

The sample consisted of isolated CdSe/ZnS QDs dropcast onto a flat, template-stripped Au surface that was coated with a thin Al_2O_3 layer. The QDs were further coated with an ultrathin 0.5 nm Al_2O_3 capping layer to reduce blinking and bleaching due to photo-oxidation and charging and to prevent electrical contact with the tip. The existence of single, isolated QDs was confirmed through atomic force microscopy. TESC was performed at room temperature with electrochemically etched Au nano-tips[67] that were precisely positioned using shear force feedback with ≈ 100 pm spatial control and generally held at a distance of ≈ 1 nm above the sample as shown in Figure 1a. The nano-tips were tilted at an angle of 35°, which had been shown to yield significantly increased field confinement compared to vertical geometries through breaking of the axial symmetry, which led to confinement of the longitudinal antenna mode.[65] Illumination was provided by a continuous wave HeNe laser with wavelength $\lambda = 632.8$ nm, with power ≤ 1 mW resulting in a fluence of $\leq 10^7$ W cm^{-2} at the tip through an NA = 0.8 objective lens as shown schematically in Figure 1a,top. With $\omega_{\mathrm{SP}} \approx \omega_{\mathrm{QD}}$ this led to near-resonant excitation of both the cavity SPP and QD exciton, as illustrated in Figure 1a. Further experimental details are given in the Supporting Information.

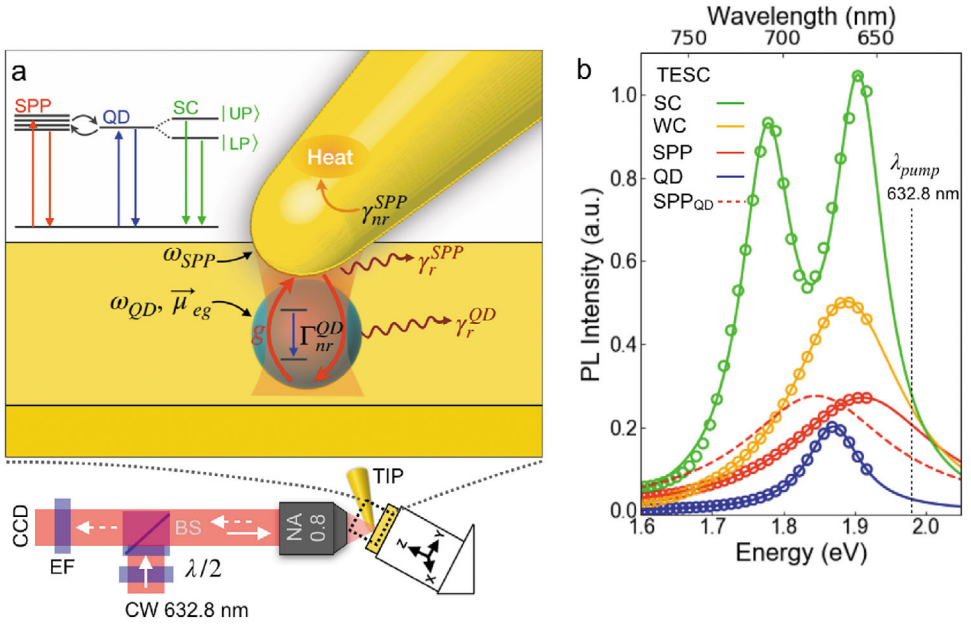

Figure 1. Tip-enhanced strong coupling (TESC) experiment and spectroscopy. a) The strongly confined $|E_z|$ fields in the plasmonic cavity with a tilted Au tip induce coupling to a single isolated CdSe/ZnS quantum dot (QD). b) Measured PL spectra for the QD, cavity plasmon (SPP), weakly coupled system (WC) and strongly coupled states (SC) with coupling strength $g = 141 \pm 4$ meV. A Lorentzian lineshape representing the redshifted plasmon resonance in the presence of the QD is calculated from the fitted values and is also shown (SPP$_{QD}$).

4. Experimental Results

TESC experiments are performed by first characterizing the PL spectrum from the isolated QD and from the surface plasmon (SPP) resonance of the bare plasmonic cavity, which arises from interband recombination of *d*-band holes and *sp*-band electrons and intraband transitions that are resonantly enhanced through surface plasmon excitation.[68] The measured SPP and QD spectra for tip-QD distance greater than 1 μm, that is, in the absence of near-field coupling, are shown in blue and red in Figure 1b, along with fits to Lorentzian lineshapes that yield peak energies of $\omega_{SP} = 1.91$ eV and $\omega_{QD} = 1.87$ eV and widths of $\gamma_{SP} = 125$ meV and $\gamma_{QD} = 46$ meV. These numbers are typical for plasmonic structures in which the harmonic electron oscillations predicted by the Drude model for free space are modified by the boundary conditions of the metal, and for QDs whose exciton energy changes depending on particle size due to excitonic confinement. Approaching the tip toward the quantum dot, with the onset of near-field coupling, TEPL of the QD is observed to broaden and become more intense in the weak coupling regime as shown in gold in Figure 1b.

As the tip becomes aligned directly over the emitter, splitting of the PL spectrum is observed, as shown in Figure 1b, green. This occurs as a result of the increased interaction strength between the tip and QD, leading to coupling between the cavity and emitter that is larger than the combined radiative and nonradiative cavity and emitter loss rates κ. This causes the plasmon and exciton modes to hybridize, leading to peaks associated with the ($|UP\rangle$) and ($|LP\rangle$) polariton branches, as predicted by Equation (4).

The spectrum for the strongly coupled system is fit to the solutions of the interaction Hamiltonian for a quantized radiation field interacting with a two-level emitter located at the antinode of the field in an optical microcavity in the Weisskopf–Wigner approximation following the method of Cui and Raymer[69] (for further details, see Supporting Information IV) with spectral signature given by

$$I_{PL}(\omega) = \frac{\gamma_{QD}}{2\pi} \times \left| \frac{\gamma_{SP}/2 - i(\omega - \omega_{SP})}{((\gamma_{SP} + \gamma_{QD})/4 + i(\delta)/2 - i(\omega - \omega_{QD}))^2 + \Omega_R)^2} \right|^2 \quad (12)$$

with total cavity and emitter loss rates $\gamma_{SP} = \gamma_r^{SP} + \gamma_{nr}^{SP}$ and $\gamma_{QD} = \gamma_r^{QD} + \gamma_{nr}^{QD}$, detuning $\delta = \omega_{SP} - \omega_{QD}$ for resonance frequencies ω_{SP} and ω_{QD}, and vacuum Rabi frequency Ω_R as fit parameters. The coupling strength $g = 141 \pm 4$ meV can then be extracted from these fit parameters using

$$g = 2\sqrt{\Omega_R^2 - \frac{(\omega_{QD} - \omega_{SP})^2}{4} + \frac{(\gamma_{SP} - \gamma_{QD})^2}{16}} \quad (13)$$

While the bare tip plasmonic cavities without QD generally have higher resonance frequencies than the QDs by ≈ 50 meV, the emitter-coupled cavity emission is redshifted by $\approx 2\%$ due to the modified local dielectric environment and the increased tip-substrate separation. This leads to improved resonance matching of the QD with the nano-cavity ($\omega_{QD} \approx \omega_{spp(QD)}$), as seen by plotting the shifted SPP spectrum based on the fitted cavity parameters in the strong coupling regime (Figure 1b, red dashed).[70]

A thorough survey of TESC spectra for many individual QDs reveals a broad distribution of coupling strengths for

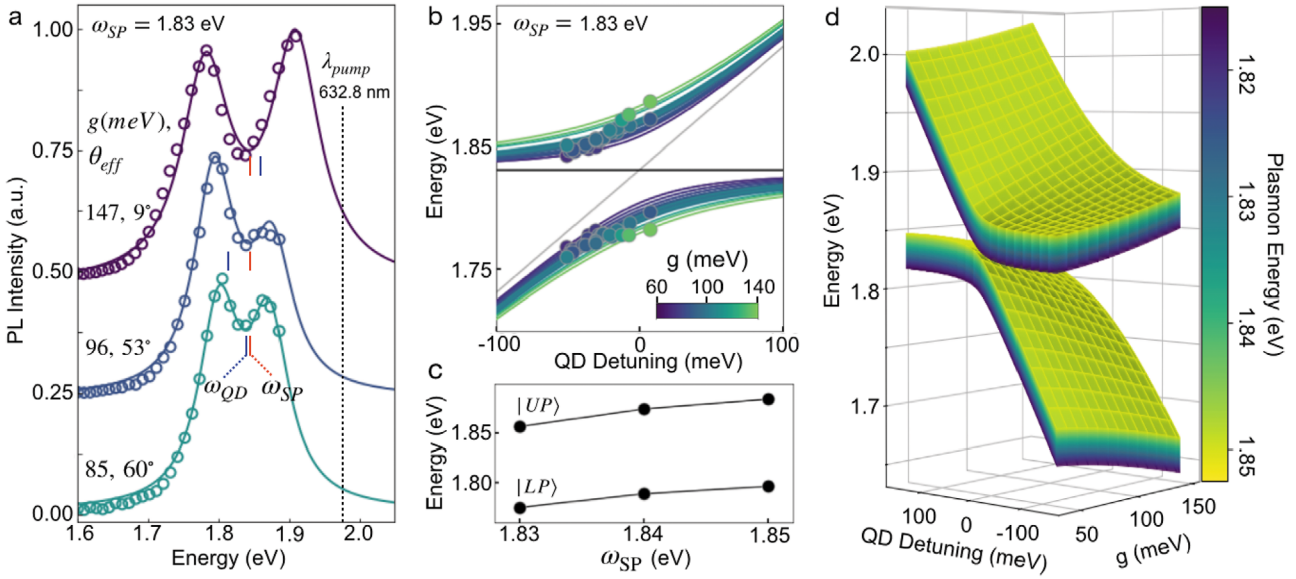

Figure 2. Anticrossing observed across a three dimensional parameter space. a) Examples of spectral variation arising from changes in coupling strength and detuning for different QDs measured with the same plasmonic cavity with ω_{SP} = 1.83 meV. b) Anticrossing curve showing mode dispersion with QD detuning and coupling strength (color bar) for a representative cavity with ω_{SP} = 1.83 eV. c) Average $|UP\rangle$ and $|LP\rangle$ energies for cavities with increasing ω_{SP}. d) Calculated mode surfaces and their dependence on detuning, coupling strength, and plasmon energy.

different QDs, with a maximum achievable coupling strength of $g \approx 150$ meV, as shown by the representative spectra in **Figure 2**a. We consistently achieve these large coupling strengths because of the ability to optimize the spatial position of the tip with respect to the QD. The variation in coupling strengths between different QDs is likely due to the random orientation of the QD dipole moment $\vec{\mu}_{eg}$ with respect to the cavity field axis $\vec{E}$. In addition, minor contributions may come from local variations in the sample geometry, such as the thickness of the Al_2O_3 coating and the roughness of the underlying Au. We can describe the combination of these effects by introducing an effective dipole orientation θ_{eff} which accounts for both the minor local variations in sample structure and the dominant effect of the deviation of the QD dipole moment from the surface normal cavity field, in which case $\hbar g = |\vec{\mu}_{eg}||\vec{E}| \cos\theta_{eff}$. Examples of this variation in θ_{eff} and corresponding fits are shown in Figure 2a.

In addition, the detuning of different QDs coupled to a specific tip-cavity $\delta = (\omega_{SP} - \omega_{QD})$ is observed to vary by ≈ 50 meV due to intrinsic variation in the QD emission energy based on the QD structure and local environment.

This variation in emission energy for different QDs allows us to build anticrossing curves through sequential measurements of different QDs using the same plasmonic nano-cavity. A series of TEPL spectra from 28 strongly coupled QDs with increasing cavity detuning are each fit to Equation (4) to derive the peak energies $|UP\rangle$ and $|LP\rangle$ and detuning δ of the QD spectrum. Figure 2b shows the resulting spectral dispersion, which reveals anticrossing behavior. The corresponding theoretical dispersion of the polariton modes as a function of cavity detuning are given by the solutions to Equation (4), and plotted using the fitted values of ω_{SP}, ω_{QD}, γ_{SP}, γ_{QD}, and Ω (solid lines, Figure 2b). The variation in QD coupling strength g manifests itself as a variation in the energy gap between the $|UP\rangle$ and $|LP\rangle$ states, and is depicted by the color scale for g. The resonance energies of plasmonic cavities depends on their specific geometry, and while ω_{SP} of the nano-tips shows only limited spectral variation from tip to tip of < 20 meV, this still allows for characterization of anticrossing along the cavity resonance dimension in addition to QD detuning. In extension of our previous work, examples of anticrossing behavior for plasmonic cavities with intrinsic resonances ranging from ω_{SP} = 1.83 eV to ω_{SP} = 1.85 are shown in Figure S2, Supporting Information. The average $|UP\rangle$ and $|LP\rangle$ energies for QDs measured with each cavity exhibit the the expected linear shift with increasing ω_{SP} energy as shown in Figure 2c.

As an overview, Figure 2d shows modeled dispersion behavior of our system over a 3D parameter space which includes QD detuning, cavity resonance, and coupling strength, based on the aggregate of TESC data over the transition from weak to strong coupling.

Finally, by taking advantage of the ability to position the scanning nano-cavity with nm precision, we investigate the dependence of the coupling strength on the relative tip-QD position. **Figure 3** shows the variations in the PL spectra (a) and resulting coupling strength (c) for increasing lateral tip position with respect to the center of the QD (x-direction). Similar data along the orthogonal y direction are given in Figure S1, Supporting Information. Figure 3b shows the spectral variation and rapid fall-off of the corresponding coupling strength (d) as the tip is retracted from above the QD in the vertical z direction. These results show that cavity formation occurs over a longer length scale for the in-plane compared to the out-of-plane direction. This behavior can be understood by considering that the finite tip with radius $r_{tip} \approx 5$ nm continues to interact with the QD with radius $r_{QD} \approx 4$ nm as it is scanned laterally and a constant tip-sample

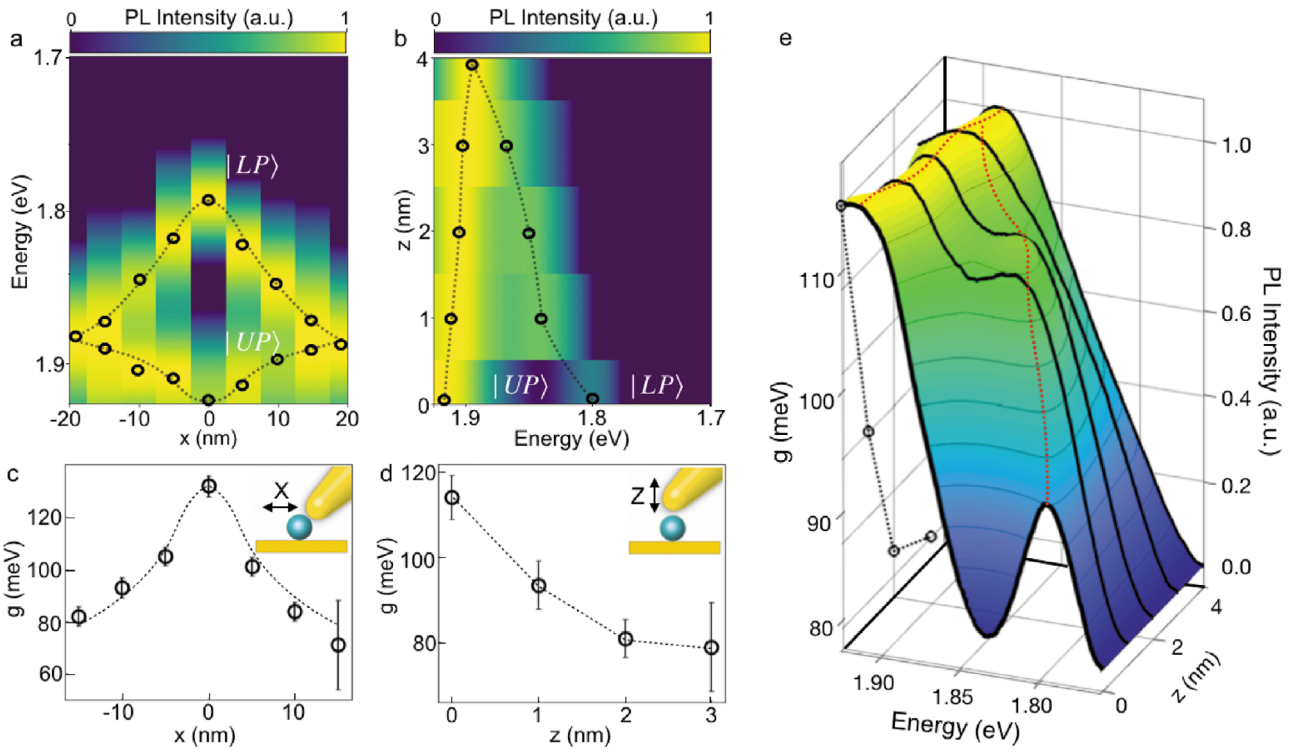

Figure 3. Active control of tip-induced single quantum dot strong coupling. Tip-enhanced photoluminesence spectra as the a) lateral and b) vertical cavity-sample separation distance is scanned, and c,d) corresponding coupling strength fit values (circles). e) 3D rendering of the data from (b) and (d). Dashed lines are provided as a guide to the eye.

separation distance is maintained. This leads to continuous reformation of the cavity, maintaining strong confinement and coupling to the QD until a lateral distance of $r_{tip} + r_{QD}$. In contrast, the tight confinement of the cavity mode volume is rapidly lost when the tip is retracted vertically, leading to a rapid decrease of the coupling strength over distances at the single-nanometer scale. A 3D rendering of the the data from Figure 3b and (d) is shown in Figure 3e, highlighting this effect.

5. Theoretical Modeling

In order to confirm the intuitive explanation given above for the significantly different length scales over which cavity-QD coupling varies as the tip is scanned in the lateral as compared to the vertical direction we simulate the coupled system numerically. Our first approach is to explicitly calculate the scattering spectrum for the entire coupled system, to fit the spectrum in order to obtain the coupling strength, g, and to repeat the process for a number of different tip positions. We perform the calculations using the finite-element method (FEM), because FEM solvers readily incorporate variable meshing, making it possible to handle the large range of length scales in the system. Details on the FEM calculations are given in the Supporting Information.

Maps of the electric field for lateral tip displacements of −5, −10, and −15 nm are shown in **Figure 4**a–c. It can be seen that lateral displacement of the tip away from the center of the QD does not simply move the local field across the QD. Rather, the displacement leads to reconfiguration of the confined field, resulting in a new cavity for each tip position. As long as the tip is in contact with the QD, the electric field E is still localized, with the degree of localization decreasing gradually as the tip moves laterally. The nanocavity forms as a result of the interaction of all three components: the tip, the substrate, and the QD.

The calculated dependence of g on the lateral tip position is shown in Figure 4d. The relatively slow decay with lateral displacement scaling on the order of the combined tip and QD radius is in good agreement with the experimental results in Figure 3a. Quantitative differences between theory and experiment are likely due to differences between the assumed tip geometry in the FEM simulations compared to the actual tip geometry.

The FEM simulations can also be used to understand the faster decay of g with vertical displacement of the tip, as shown in Figure 4e–h. In this case, the tip loses near-field contact with the QD quickly upon retraction. Rather than reconfiguring, the field simply becomes less confined, resulting in a rapid decline in the coupling strength on a length scale shorter than the tip radius.

Although these FEM calculations provide insight into the TESC system, they are computationally demanding, requiring an independent calculation to be performed for each tip position. A more computationally efficient approach, which also provides additional physical insight, is to use a quasinormal mode (QNM) framework.[11,71,72] In this approach, FEM simulations are used not to calculate scattering spectra, but to calculate the complex effective mode volumes $\tilde{V}$ for the quasinormal modes of the tip-substrate system. The same tip and substrate geometry is used as in the previous FEM simulations, but the QD is modeled as a point dipole, rather than an extended dielectric sphere. This

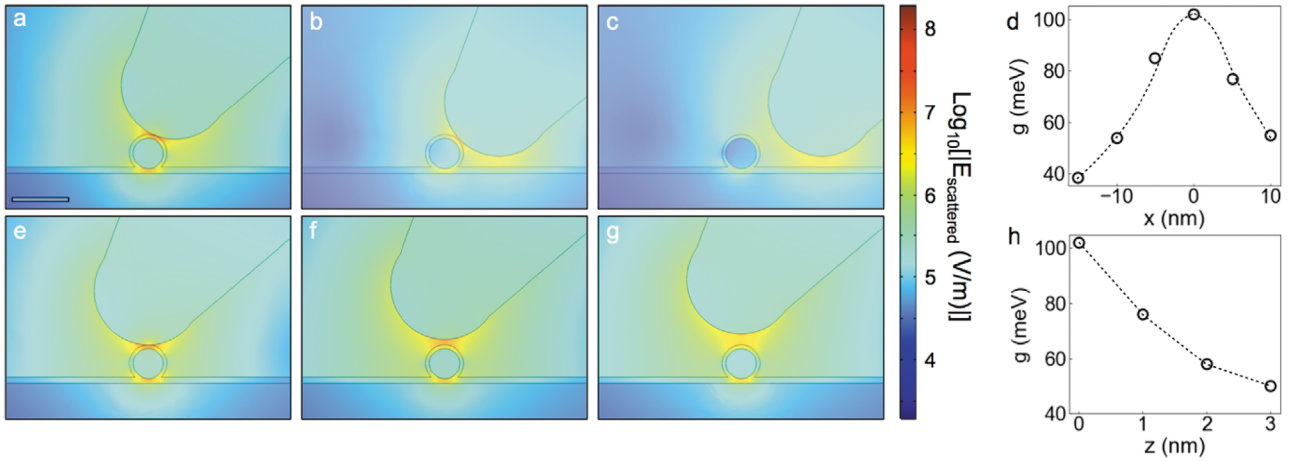

Figure 4. Simulation of cavity field and coupling strength. a–c) Electric field for lateral translations of −5 nm, −10 nm, and −15 nm with a 2 nm gap maintained between tip and substrate. The scale bar is 10 nm. d) Corresponding coupling strength obtained by fitting scattering spectra at each lateral displacement with dashed line as a guide to the eye. e–g) Electric field for vertical displacements of 0, 2, and 4 nm, respectively, and h) corresponding coupling strength obtained by fitting scattering spectra at each vertical displacement with dashed line as a guide to the eye.

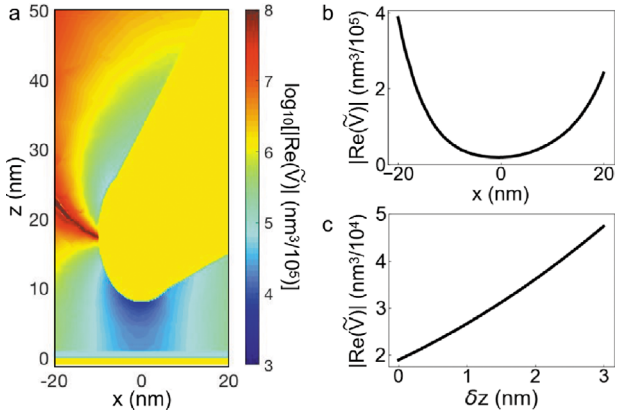

Figure 5. QNM modeling of cavity mode volume. a) Mapping of Re[$\tilde{V}$] for the principle cavity mode, with a tip-sample separation of 8 nm. b) Lateral cross-section of the mode volume map showing increasing mode volume over a displacement of ≈ 20 nm. c) Optimized mode volumes for increasing tip height δz compared to its original position.

enables a single calculation to return maps of the QNM mode volume as a function of position around the tip. The tradeoff for this ability to maintain generality of the results at all positions in space is that the quantitative values of the mode volumes will be larger than the experimental values, because the dielectric material between the tip and substrate is not taken into account. Futher details on the QNM calculations are given in the Supporting Information.

Figure 5a shows a map of $Re[\tilde{V}]$ for the principle mode, at a tip-sample separation of 8 nm. A cross-section through the map shows that the mode volume increases over a distance of ≈ 20 nm as the dipole is moved away from the center of the tip in the lateral direction, as shown in Figure 5b. Furthermore, the mode volume was mapped for increasing tip height δz compared to its original position, as shown in Figure 5c, revealing a tightly confined cavity field which decays rapidly with vertical displacement. Assuming that the QD couples only to this principle QNM, the mode volumes can be converted into coupling strengths approximately using Equation (8), above, or more exactly using Eq. (8.4) of Ref. [11].

6. Discussion

The ability to precisely control the relative cavity–emitter position in TESC enables large single-emitter coupling strengths of $g \approx 150$ meV that are comparable even to those achieved using large ensembles of emitters,[54,66] and are significantly larger than those seen in other experiments which use DNA origami and configurable cavity designs to improve the coupling strength by controlling the position of an emitter within the cavity.[8,10,73] By combining this ability to precisely control the experimental geometry on the single-nanometer scale, with electromagnetic simulations of the cavity field, we also gain insight into the dynamics of cavity formation as the tip-emitter-substrate geometry is varied in a well-defined manner. This reveals that, as the tip is scanned across the QD, field localization is maintained, decreasing only moderately as the tip is displaced from its optimal position. The evolving tip-emitter-substrate geometry causes the cavity mode to be reconfigured, leading to formation of a unique cavity at each position. Conversely, when the tip is retracted vertically, the field confinement is lost, leading to rapidly increasing mode volume and a corresponding fall-off in the coupling strength.

The simulated cavity distributions also indicate that there is a significant field gradient due to the finite size of the QD. It has been shown that in this regime, the point dipole approximation breaks down and that new, higher order optical transitions become allowed that can significantly enhance the light matter interaction strength. [74] This effect may be an enabling factor that allows us to achieve the large coupling strengths achieved here.

Furthermore, TESC allows direct comparison of coupling parameters for individual emitters coupled to the same plasmonic cavity. This increases experimental flexibility enabling, for example, measurement of anticrossing curves through addressing

different emitters with intrinsically varying cavity detuning δ instead of changing fundamental experimental parameters like laser power or temperature that can impact the underlying system properties.[3,54,75] One can envision a broad range of new experiments based on this flexibility, such as TESC imaging in 2D Van der Waals materials, the investigation of randomly located single photon emitting defects in solid state systems that are difficult to probe with stationary plasmonic cavities despite their exceptional properties for quantum information and technology,[76–81] and coupling of multiple single emitters for entanglement and superradiance.[82–85] While room temperature strong coupling is feasible in nano-plasmonic cavities, it has been assumed that the strong dissipation and dephasing introduced by the thermal vibrational reservoir at these temperatures would make them inaccessible to technologies that require quantum coherence and control of single emitter-photon states. However, recent theoretical predictions indicate that quantum properties can be preserved at room temperature through engineering the spectral properties of the surrounding environment.[86–90] The combination of configurability and ultra-strong coupling in TESC could enable systematic investigation of emitters' environmental heat bath coupling and dissipation pathways over a range of temperatures to refine system-reservoir engineering and decrease decoherence at room temperature.[91–93]

Furthermore, room temperature strong coupling could enable the development of chip-based and broadly distributable platforms for technologies based on quantum transduction and quantum-state control.[94–97] Extension of nano-cQED to the single photon limit would further enable quantum elements such as single-photon switching,[98,99] control of single photons by emitter states and single emitters by photons,[100–102] and single-photon optical transistors.[103] Additionally, coherent control of the quantum state of an emitter through time domain Rabi flopping is required for preparation and read-out of quantum states but has not yet been achieved using plasmonic nanocavities. For a typical nanocavity-emitter system with Rabi splitting of 100 meV, Rabi oscillations occur at a rate of $\approx$ 40 fs. This timescale is well within the capabilities of modern ultrafast laser systems which can achieve pulse durations down to a few fs,[104] and could be combined with TESC to allow for precise control of the emitter's state through Rabi flopping, Hahn-echo, and more complex pulse sequences.[105]

Finally, the field of cavity optomechanics has recently emerged, employing a complementary approach to cQED by focusing on controlling the interaction of light with vibrational modes of solid state resonators.[106–108] However, to achieve the few vibrational quanta interaction regime in mesoscale resonators with characteristic frequencies in the MHz–GHz range, deep cryogenic conditions are required.[109–113] On the other hand, scaling the mass of a mechanical oscillator to the atomic scale in the form of a molecular bond leads to an increase in vibrational frequency into the THz–PHz regime, where the vibrational ground state can be reached at room temperature.[114,115] This enables a new regime of room temperature molecular cavity optomechanics and indeed, the coherent interaction regime of strong coupling has been reached in micro-cavities for ensemble measurements.[116,117] While optomechanics in the regime of single-molecule vibrational strong coupling has been theoretically predicted,[118,119] and experiments have approached this limit,[120] it has not yet been reached. The reduced mode volume, precise experimental control, and increased flexibility of TESC make it a promising modality to unlock the rich quantum coherent and phase-controlled light–matter interaction regime that is expected from strong coupling to single molecular vibrations.

7. Conclusion

In summary, we measured and analyzed the effect of relative cavity-emitter separation on the cavity mode volume and the resulting coupling strength in TESC both experimentally and theoretically, which revealed that the tip forms a tightly confined cavity through interaction with the QD and substrate that is dynamically re-formed as the tip position changes. This indicates that TESC does not simply provide a passive probe of the confined cavity mode, but provides a way of investigating how strong coupling is produced in nanocavities through interaction of all components.

We employed two complementary methods to theoretically investigate the cavity's behavior. First, using FEM calculations we readily account for the finite QD size and its effect on the dielectric environment in the cavity which allows insight into the changing field distribution as the cavity is formed and re-formed for each new tip position. Furthermore, this method yields a value for the coupling strength that can be directly compared with experimental measurements. However, this method is computationally intensive, which limits the number of calculations that can be done. Conversely, QNM methods can produce full maps of the mode volume for a dipole emitter at any point in space from a single calculation. These maps can then be used to calculate parameters like mode dispersion and coupling strength analytically, but require modifications to account for finite QD size, which will be the subject of future work. For example, the QD could be modeled as a polarizability tensor of which elements are calculated from the QD's dipolar response or as an ensemble of evenly distributed Lorentz Dirac oscillators, as detailed in the Supporting Information.

This work demonstrates a new methodology for characterization and optimization of plasmonic cavities and their mode volumes. Furthermore, it reveals the significantly increased utility of configurable scanning cavities for both optimizing coupling strength and expanding the experimental parameter space of nano-cavity QED.

Supporting Information

Supporting Information is available from the Wiley Online Library or from the author.

Acknowledgements

M.A.M., K.-D.P., and M.B.R. acknowledge funding from the National Science Foundation (NSF Grant CHE 1709822). D.F., H.L., and M.P. acknowledge support from the National Institute of Standards and Technology under Award Number 14D295. T.W. and P.L. acknowledge support from Agence Nationale de la Recherche (ANR), ANR contract NOMOS (ANR-18-C824-0026-03) and ISQUAD (ANR-18-CE47-0006-04). T.W. acknowledges a fellowship from the Agence Nationale de la Recherche (ANR), ANR

contract NOMOS (ANR-18-C824-0026-03) and ISQUAD (ANR-18-CE47-0006-04). J.A.K. and T.G. acknowledge support from the National Science Foundation under grant ECCS-1407677.

Conflict of Interest

The authors declare no conflict of interest.

Author Contributions

M.B.R., M.P., and K.-D.P. conceived the experiment. M.A.M. and K.-D.P. performed the measurements. D.F. performed the FEM simulations. T.W. performed QNM modeling. H.L., J.A.K., T.G., and M.P. designed and prepared the samples. M.A.M., D.F., T.W., K.-D.P., H.L., P.L., M.P., and M.B.R. analyzed the data, and all authors discussed the results. M.A.M., and M.B.R. wrote the manuscript with contributions from all authors. M.B.R. supervised the project.

Keywords

nano-cavity quantum electrodynamics, quantum emitter, strong coupling

Received: July 24, 2019
Revised: September 27, 2019
Published online:

[1] T. Tiecke, J. D. Thompson, N. P. de Leon, L. Liu, V. Vuletić, M. D. Lukin, *Nature* **2014**, *508*, 241.
[2] H. Bernien, B. Hensen, W. Pfaff, G. Koolstra, M. S. Blok, L. Robledo, T. H. Taminiau, M. Markham, D. J. Twitchen, L. Childress, R. Hanson, *Nature* **2013**, *497*, 86.
[3] J. M. Fink, M. Goppl, M. Baur, R. Bianchetti, P. J. Leek, A. Blais, A. Wallraff, *Nature* **2008**, *454*, 315.
[4] K. M. Birnbaum, A. Boca, R. Miller, A. D. Boozer, T. E. Northup, H. J. Kimble, *Nature* **2005**, *436*, 87.
[5] D. M. Coles, Y. Yang, Y. Wang, R. T. Grant, R. A. Taylor, S. K. Saikin, A. Aspuru-Guzik, D. G. Lidzey, J. K.-H. Tang, J. M. Smith, *Nat. Commun.* **2014**, *5*, 5561.
[6] R. Chikkaraddy, B. de Nijs, F. Benz, S. J. Barrow, O. A. Scherman, E. Rosta, A. Demetriadou, P. Fox, O. Hess, J. J. Baumberg, *Nature* **2016**, *535*, 127.
[7] H. Leng, B. Szychowski, M.-C. Daniel, M. Pelton, *Nat. Commun.* **2018**, *9*, 4012.
[8] H. Groß, J. M. Hamm, T. Tufarelli, O. Hess, B. Hecht, *Sci. Adv.* **2018**, *4*, eaar4906.
[9] K.-D. Park, M. A. May, H. Leng, J. Wang, J. A. Kropp, T. Gougousi, M. Pelton, M. B. Raschke, *Sci. Adv.* **2019**, 8.
[10] O. S. Ojambati, R. Chikkaraddy, W. D. Deacon, M. Horton, D. Kos, V. A. Turek, U. F. Keyser, J. J. Baumberg, *Nat. Commun.* **2019**, *10*, 1049.
[11] P. Lalanne, W. Yan, K. Vynck, C. Sauvan, J.-P. Hugonin, *Laser Photonics Rev.* **2018**, *12*, 1700113.
[12] C. Sauvan, J. P. Hugonin, I. S. Maksymov, P. Lalanne, *Phys. Rev. Lett.* **2013**, *110*, 237401.
[13] R. Waldron, *Proceedings of the IEE Part C: Monographs* **1960**, *107*, 272.
[14] S. A. Maier, *Opt. Quantum Electron.* **2006**, *38*, 257.
[15] K. G. Cognée, W. Yan, F. La China, D. Balestri, F. Intonti, M. Gurioli, A. F. Koenderink, P. Lalanne, *Optica* **2019**, *6*, 269.
[16] A. Einstien, *Z. Phys.* **1917**, *18*, 121.
[17] S. Haroche, D. Kleppner, *Phys. Today* **1989**, *42*, 24.
[18] E. Purcell, *Phys. Rev.* **1946**, *69*, 681.
[19] N. Bloembergen, E. M. Purcell, R. V. Pound, *Phys. Rev.* **1948**, *73*, 679.
[20] M. Pelton, *Nat. Photonics* **2015**, *9*, 427.
[21] K. Drexhage, *J. Lumin.* **1970**, *1–2*, 693.
[22] G. Gabrielse, H. Dehmelt, *Phys. Rev. Lett.* **1985**, *55*, 67.
[23] P. Goy, J. M. Raimond, M. Gross, S. Haroche, *Phys. Rev. Lett.* **1983**, *50*, 1903.
[24] R. G. Hulet, E. S. Hilfer, D. Kleppner, *Phys. Rev. Lett.* **1985**, *55*, 2137.
[25] W. Jhe, A. Anderson, E. A. Hinds, D. Meschede, L. Moi, S. Haroche, *Phys. Rev. Lett.* **1987**, *58*, 666.
[26] F. D. Martini, G. Innocenti, G. R. Jacobovitz, P. Mataloni, *Phys. Rev. Lett.* **1987**, *59*, 2955.
[27] D. J. Heinzen, J. J. Childs, J. E. Thomas, M. S. Feld, *Phys. Rev. Lett.* **1987**, *58*, 1320.
[28] G. Rempe, H. Walther, N. Klein, *Phys. Rev. Lett.* **1987**, *58*, 353.
[29] M. Brune, J. M. Raimond, P. Goy, L. Davidovich, S. Haroche, *Phys. Rev. Lett.* **1987**, *59*, 1899.
[30] L. S. Brown, G. Gabrielse, K. Helmerson, J. Tan, *Phys. Rev. Lett.* **1985**, *55*, 44.
[31] A. Liebman, G. J. Milburn, *Phys. Rev. A* **1995**, *51*, 736.
[32] D. Meschede, H. Walther, G. Müller, *Phys. Rev. Lett.* **1985**, *54*, 551.
[33] G. Kurizki, *Phys. Rev. A* **1990**, *42*, 2915.
[34] J. J. Sanchez-Mondragon, N. B. Narozhny, J. H. Eberly, *Phys. Rev. Lett.* **1983**, *51*, 550.
[35] Y. Zhu, D. J. Gauthier, S. E. Morin, Q. Wu, H. J. Carmichael, T. W. Mossberg, *Phys. Rev. Lett.* **1990**, *64*, 2499.
[36] M. G. Raizen, R. J. Thompson, R. J. Brecha, H. J. Kimble, H. J. Carmichael, *Phys. Rev. Lett.* **1989**, *63*, 240.
[37] C. Weisbuch, M. Nishioka, A. Ishikawa, Y. Arakawa, *Phys. Rev. Lett.* **1992**, *69*, 3314.
[38] J. Gerard, B. Sermage, B. Gayral, B. Legrand, E. Costard, V. Thierry-Mieg, *Phys. Rev. Lett.* **1998**, *81*, 1110.
[39] M. Bayer, T. L. Reinecke, F. Weidner, A. Larionov, A. McDonald, A. Forchel, *Phys. Rev. Lett.* **2001**, *86*, 3168.
[40] J. P. Reithmaier, G. Sek, A. Löffler, C. Hofmann, S. Kuhn, S. Reitzenstein, L. V. Keldysh, V. D. Kulakovskii, T. L. Reinecke, A. Forchel, *Nature* **2004**, *432*, 197.
[41] J. R. Buck, H. J. Kimble, *Phys. Rev. A* **2003**, *67*, 033806.
[42] T. Aoki, B. Dayan, E. Wilcut, W. P. Bowen, A. S. Parkins, T. J. Kippenberg, K. J. Vahala, H. J. Kimble, *Nature* **2006**, *443*, 671.
[43] N. Tkachenko, *Optical Spectroscopy: Methods and Instrumentations*, Elsevier B.V., Amsterdam, Oxford **2006**.
[44] V. Giannini, A. I. Fernández-Domínguez, Y. Sonnefraud, T. Roschuk, R. Fernández-García, S. A. Maier, *Small* **2010**, *6*, 2498.
[45] L. Novotny, N. van Hulst, *Nat. Photonics* **2011**, *5*, 83.
[46] P. Bharadwaj, B. Deutsch, L. Novotny, *Adv. Opt. Photonics* **2009**, *1*, 438.
[47] E. Synge, *The London, Edinburgh, Dublin Philos. Mag. J. Sci.* **1932**, *13*, 297.
[48] U. C. Fischer, D. W. Pohl, *Phys. Rev. Lett.* **1989**, *62*, 458.
[49] W. R. Holland, D. G. Hall, *Phys. Rev. B* **1983**, *27*, 7765.
[50] B. Rothenhiiusler, W. Knollt, *Nature* **1988**, *332*, 615.
[51] R. Chikkaraddy, B. de Nijs, F. Benz, S. J. Barrow, O. A. Scherman, E. Rosta, A. Demetriadou, P. Fox, O. Hess, J. J. Baumberg, *Nature* **2016**, *535*, 127.
[52] A. Manjavacas, F. G. d. Abajo, P. Nordlander, *Nano Lett.* **2011**, *11*, 2318.
[53] M. Wersäll, J. Cuadra, T. J. Antosiewicz, S. Balci, T. Shegai, *Nano Lett.* **2017**, *17*, 551.
[54] M. Wersäll, J. Cuadra, T. J. Antosiewicz, S. Balci, T. Shegai, *Nano Lett.* **2016**, *17*, 551.
[55] A. Reiserer, N. Kalb, G. Rempe, S. Ritter, *Nature* **2014**, *508*, 237.

[56] D. Fattal, K. Inoue, J. Vučković, C. Santori, G. S. Solomon, Y. Yamamoto, *Phys. Rev. Lett.* **2004**, *92*, 037903.
[57] J. M. Fink, M. Göppl, M. Baur, R. Bianchetti, P. J. Leek, A. Blais, A. Wallraff, *Nature* **2008**, *454*, 315.
[58] H. U. Yang, R. L. Olmon, K. S. Deryckx, X. G. Xu, H. A. Bechtel, Y. Xu, B. A. Lail, M. B. Raschke, *ACS Photonics* **2014**, *1*, 894.
[59] M. B. Raschke, S. Berweger, J. M. Atkin, in *Plasmonics: Theory and Applications* (Eds: T. V. Shahbazyan, M. I. Stockman), Springer, Netherlands, Dordrecht **2013**, pp. 237–281.
[60] Q. Zhu, S. Zheng, S. Lin, T.-R. Liu, C. Jin, *Nanoscale* **2014**, *6*, 7237.
[61] N. Behr, M. B. Raschke, *J. Phys. Chem. C* **2008**, *112*, 3766.
[62] R. M. Roth, N. C. Panoiu, M. M. Adams, R. M. Osgood, C. C. Neacsu, M. B. Raschke, *Opt. Express* **2006**, *14*, 2921.
[63] K.-D. Park, O. Khatib, V. Kravtsov, G. Clark, X. Xu, M. B. Raschke, *Nano Lett.* **2016**, *16*, 2621.
[64] K.-D. Park, T. Jiang, G. Clark, X. Xu, M. B. Raschke, *Nat. Nanotechnol.* **2018**, *13*, 59.
[65] K.-D. Park, M. B. Raschke, *Nano Lett.* **2018**, *18*, 2912.
[66] D. Melnikau, R. Esteban, D. Savateeva, A. Sánchez-Iglesias, M. Grzelczak, M. K. Schmidt, L. M. Liz-Marzán, J. Aizpurua, Y. P. Rakovich, *J. Phys. Chem. Lett.* **2016**, *7*, 354.
[67] C. Neacsu, G. Steudle, M. Raschke, *Appl. Phys. B* **2005**, *80*, 295.
[68] V. Kravtsov, S. Berweger, J. M. Atkin, M. B. Raschke, *Nano Lett.* **2014**, *14*, 5270.
[69] G. Cui, M. G. Raymer, *Phys. Rev. A* **2006**, *73*, 5.
[70] T. R. Jensen, M. L. Duval, K. L. Kelly, A. A. Lazarides, G. C. Schatz, R. P. Van Duyne, *J. Phys. Chem. B* **1999**, *103*, 9846.
[71] W. Yan, R. Faggiani, P. Lalanne, *Phys. Rev. B* **2018**, *97*, 205422.
[72] Simulations were performed with the COMSOL-based solver QNMEig [71] of the QNM open-source package MAN (Modal Analysis of Nanoresonators) that can be downloaded at https://www.lp2n.institutoptique.fr/light-complex-nanostructures.
[73] R. Chikkaraddy, V. A. Turek, N. Kongsuwan, F. Benz, C. Carnegie, T. van de Goor, B. de Nijs, A. Demetriadou, O. Hess, U. F. Keyser, J. J. Baumberg, *Nano Lett.* **2018**, *18*, 405.
[74] M. L. Andersen, S. Stobbe, A. S. Sørensen, P. Lodahl, *Nat. Phys.* **2011**, *7*, 215.
[75] S. Münch, S. Reitzenstein, P. Franeck, A. Löffler, T. Heindel, S. Hüfling, L. Worschech, A. Forchel, *Opt. Express* **2009**, *17*, 12821.
[76] L. J. Rogers, K. D. Jahnke, M. W. Doherty, A. Dietrich, L. P. McGuinness, C. Müller, T. Teraji, H. Sumiya, J. Isoya, N. B. Manson, F. Jelezko, *Phys. Rev. B* **2014**, *89*, 235101.
[77] J. B. Pérez, J. C. Arce, *J. Chem. Phys.* **2018**, *148*, 214302.
[78] X. Meng, Y. Zheng, *J. Phys. B: At., Mol. Opt. Phys.* **2014**, *47*, 065501.
[79] C. L. Degen, *Appl. Phys. Lett.* **2008**, *92*, 243111.
[80] S. Kumar, A. Kaczmarczyk, B. D. Gerardot, *Nano Lett.* **2015**, *15*, 7567.
[81] T. T. Tran, K. Bray, M. J. Ford, M. Toth, I. Aharonovich, *Nat. Nanotechnol.* **2015**, *11*, 37.
[82] K. Cong, Q. Zhang, Y. Wang, G. T. Noe, A. Belyanin, J. Kono, *J. Opt. Soc. Am. B* **2016**, *33*, C80.
[83] P. C. Cárdenas, N. Quesada, H. Vinck-Posada, B. A. Rodríguez, *J. Phys.: Condens. Matter* **2011**, *23*, 265304.
[84] N. Quesada, *Phys. Rev. A* **2012**, *86*, 1.
[85] M. Calic, C. Jarlov, P. Gallo, B. Dwir, A. Rudra, E. Kapon, *Sci. Rep.* **2017**, *7*, 1.
[86] S. Deffner, E. Lutz, *Phys. Rev. Lett.* **2011**, *107*, 140404.
[87] F. Impens, D. Guéry-Odelin, *Sci. Rep.* **2019**, *9*, 4048.
[88] P. Zanardi, L. Campos Venuti, *Phys. Rev. Lett.* **2014**, *113*, 240406.
[89] S. Touzard, A. Grimm, Z. Leghtas, S. Mundhada, P. Reinhold, C. Axline, M. Reagor, K. Chou, J. Blumoff, K. Sliwa, S. Shankar, L. Frunzio, R. Schoelkopf, M. Mirrahimi, M. Devoret, *Phys. Rev. X* **2018**, *8*, 021005.
[90] F. Pastawski, L. Clemente, J. I. Cirac, *Phys. Rev. A* **2011**, *83*, 012304.
[91] L. Cui, W. Jeong, S. Hur, M. Matt, J. C. Klöckner, F. Pauly, P. Nielaba, J. C. Cuevas, E. Meyhofer, P. Reddy, *Science* **2017**, *355*, 1192.
[92] R. Moghaddasi Fereidani, D. Segal, *J. Chem. Phys.* **2019**, *150*, 024105.
[93] R. Miao, H. Xu, M. Skripnik, L. Cui, K. Wang, K. G. L. Pedersen, M. Leijnse, F. Pauly, K. Wärnmark, E. Meyhofer, P. Reddy, H. Linke, *Nano Lett.* **2018**, *18*, 5666.
[94] D. Englund, A. Faraon, I. Fushman, N. Stoltz, P. Petroff, J. Vučković, *Nature* **2007**, *450*, 857.
[95] K. Srinivasan, O. Painter, *Nature* **2007**, *450*, 862.
[96] P. Lodahl, S. Mahmoodian, S. Stobbe, *Rev. Mod. Phys.* **2015**, *87*, 347.
[97] C. U. Lei, W.-M. Zhang, *Phys. Rev. A* **2011**, *84*, 052116.
[98] D. Englund, A. Majumdar, M. Bajcsy, A. Faraon, P. Petroff, J. Vučković, *Phys. Rev. Lett.* **2012**, *108*, 093604.
[99] T. Volz, A. Reinhard, M. Winger, A. Badolato, K. J. Hennessy, E. L. Hu, A. Imamoğlu, *Nat. Photonics* **2012**, *6*, 605.
[100] H. Kim, R. Bose, T. C. Shen, G. S. Solomon, E. Waks, *Nat. Photonics* **2013**, *7*, 373.
[101] C. Arnold, J. Demory, V. Loo, A. Lemaître, I. Sagnes, M. Glazov, O. Krebs, P. Voisin, P. Senellart, L. Lanco, *Nat. Commun.* **2015**, *6*, 6236.
[102] S. Sun, H. Kim, G. S. Solomon, E. Waks, *Nat. Nanotechnol.* **2016**, *11*, 539.
[103] S. Sun, H. Kim, Z. Luo, G. S. Solomon, E. Waks, *Science* **2018**, *361*, 57.
[104] V. Kravtsov, R. Ulbricht, J. M. Atkin, M. B. Raschke, *Nat. Nanotechnol.* **2016**, *11*, 459.
[105] C. Degen, F. Reinhard, P. Cappellaro, *Rev. Mod. Phys.* **2017**, *89*, 035002.
[106] M. Aspelmeyer, T. J. Kippenberg, F. Marquardt, *Rev. Mod. Phys.* **2014**, *86*, 1391.
[107] T. J. Kippenberg, K. J. Vahala, *Science* **2008**, *321*, 1172.
[108] M. Metcalfe, *Appl. Phys. Rev.* **2014**, *1*, 031105.
[109] E. E. Wollman, C. U. Lei, A. J. Weinstein, J. Suh, A. Kronwald, F. Marquardt, A. A. Clerk, K. C. Schwab, *Science* **2015**, *349*, 952.
[110] R. Riedinger, S. Hong, R. A. Norte, J. A. Slater, J. Shang, A. G. Krause, V. Anant, M. Aspelmeyer, S. Gröblacher, *Nature* **2016**, *530*, 313.
[111] R. Riedinger, A. Wallucks, I. Marinković, C. Löschnauer, M. Aspelmeyer, S. Hong, S. Gröblacher, *Nature* **2018**, *556*, 473.
[112] C. F. Ockeloen-Korppi, E. Damskägg, J.-M. Pirkkalainen, M. Asjad, A. A. Clerk, F. Massel, M. J. Woolley, M. A. Sillanpää, *Nature* **2018**, *556*, 478.
[113] Y. Chu, P. Kharel, T. Yoon, L. Frunzio, P. T. Rakich, R. J. Schoelkopf, *Nature* **2018**, *563*, 666.
[114] M. K. Dezfouli, R. Gordon, S. Hughes, *ACS Photonics* **2019**, *6*, 1400.
[115] F. Benz, M. K. Schmidt, A. Dreismann, R. Chikkaraddy, Y. Zhang, A. Demetriadou, C. Carnegie, H. Ohadi, B. de Nijs, R. Esteban, J. Aizpurua, J. J. Baumberg, *Science* **2016**, *354*, 726.
[116] A. Fainstein, N. D. Lanzillotti-Kimura, B. Jusserand, B. Perrin, *Phys. Rev. Lett.* **2013**, *110*, 037403.
[117] J. George, S. Wang, T. Chervy, A. Canaguier-Durand, G. Schaeffer, J.-M. Lehn, J. A. Hutchison, C. Genet, T. W. Ebbesen, *Faraday Discuss.* **2015**, *178*, 281.
[118] P. Roelli, C. Galland, N. Piro, T. J. Kippenberg, *Nat. Nanotechnol.* **2016**, *11*, 164.
[119] M. K. Schmidt, R. Esteban, A. González-Tudela, G. Giedke, J. Aizpurua, *ACS Nano* **2016**, *10*, 6291.
[120] A. Lombardi, M. K. Schmidt, L. Weller, W. M. Deacon, F. Benz, B. de Nijs, J. Aizpurua, J. J. Baumberg, *Phys. Rev. X* **2018**, *8*, 011016.